Predictions and sensitivity forecasts for reionization-era [C II] line intensity mapping

Sebastian Dumitru[1,2,3]★, Girish Kulkarni[1,2,4]†, Guilaine Lagache[5] and Martin G. Haehnelt[1,2]

[1]*Institute of Astronomy and Kavli Institute of Cosmology, University of Cambridge, Madingley Road, Cambridge CB3 0HA, UK*
[2]*Kavli Institute of Cosmology, University of Cambridge, Madingley Road, Cambridge CB3 0HA, UK*
[3]*Department of Physics and Astronomy, University of Pennsylvania, Philadelphia PA 19104, USA*
[4]*Department of Theoretical Physics, Tata Institute of Fundamental Research, Homi Bhabha Road, Mumbai 400005, India*
[5]*Aix Marseille Univ, CNRS, LAM, Laboratoire d'Astrophysique de Marseille, Marseille, France*

ABSTRACT

Observations of the high-redshift Universe using the 21 cm line of neutral hydrogen and complimentary emission lines from the first galaxies promise to open a new door for our understanding of the epoch of reionization. We present predictions for the [C II] 158 μm line and H I 21 cm emission from redshifts $z = 6$–9 using high-dynamic-range cosmological simulations combined with semi-analytical models. We find that the CONCERTO experiment should be able to marginally detect the large scale power spectrum of [C II] emission to redshifts of up to $z = 8$ (signal-to-noise ratio ~ 1 at $k < 0.1$ h/cMpc with 1500 hr of integration). A Stage II experiment similar to CCAT-p should be able to detect [C II] from even higher redshifts to high significance for similar integration times (signal-to-noise ratio of ~ 50 at $k = 0.2$ h/cMpc at $z = 6$). We study the possibility of combining such future [C II] measurements with 21 cm measurements using LOFAR and SKA to measure the [C II]-21cm cross power spectra, and find that a Stage II experiment should be able to measure the cross-power spectrum for $k \lesssim 1$ h/cMpc to signal-to-noise ratio of better than 10. We discuss the capability of such measurements to constrain astrophysical parameters relevant to reionization and show that a measurement of the [C II]-21cm cross power spectrum helps break the degeneracy between the mass and brightness of ionizing sources.

Key words: dark ages, reionization, first stars – galaxies: high-redshift – intergalactic medium

1 INTRODUCTION

Atomic and molecular emission lines with wavelength redward of hydrogen Lyman-α have the desirable property of remaining visible deep into the epoch of hydrogen reionization (redshift $z = 6$–10), where the Lyα line is difficult to observe due to saturated absorption. These emission lines, which depend on the cold gas content, the ionising radiation field, or the metallicity, uniquely probe the formation of the very first stars and galaxies. They should be a good tracer of the cosmic density structure.

Intensity mapping of such emission lines (e.g., O I, O III, C II, CO, H I, H₂) is an attractive tool to study the high-redshift Universe (Suginohara et al. 1999; Visbal & Loeb 2010; Carilli 2011; Gong et al. 2011; Lidz et al. 2011; Gong et al. 2012, 2013; Silva et al. 2015; Yue et al. 2015; Serra et al. 2016; Fonseca et al. 2017). By measuring large-scale variations in line emission from many individual unresolved galaxies, intensity mapping provides a statistical measurement that encodes cosmological and astrophysical information. This capacity of intensity mapping experiments is particularly important at redshifts corresponding to the epoch of reionization, which is a key period in the history of the Universe, when the earliest galaxies and quasars form and ionize the surrounding neutral hydrogen. Constraints from the evolution in the Lyα opacity of the intergalactic medium (IGM; e.g., Fan et al. 2006; Ota et al. 2017) and the temperature and polarization anisotropy in the cosmic microwave background (CMB; Planck Collaboration 2016) suggest that reionization occurs at redshifts $z \sim 6$–15. However, the nature of the sources of reionization remains uncertain. Measurements of the escape fraction of Lyman-continuum photons necessary for reionization from high-redshift galaxies

★ Email: sdumitru@sas.upenn.edu
† Email: kulkarni@theory.tifr.res.in

are still elusive. Although galaxies down to rest-frame UV magnitudes of $M_{\rm UV} = -12.5$ ($L \sim 10^{-3}L^*$) at redshift $z = 6$ (Livermore et al. 2017) and redshifts as high as $z = 11.1$ (Oesch et al. 2016) have been observed, the escape fraction of Lyman-continuum photons has been measured in only a handful of bright ($L > 0.5L^*$) and low-redshift ($z < 4$) galaxies. In these galaxies, the escape fraction is typically found to be 2–20% (Vanzella et al. 2010; Boutsia et al. 2011; Siana et al. 2015; Mostardi et al. 2015; Grazian et al. 2016; Japelj et al. 2017; Micheva et al. 2017) but reionization requires escape fractions of about 20% in galaxies down to $M_{\rm UV} = -13$ (Finkelstein 2016; Robertson et al. 2015; Khaire et al. 2016). There is tentative evidence for a dominant contribution to reionization from quasars from the suggestion of a rather steep faint end of the QSO luminosity function at high redshift by Giallongo et al. (2015), and large Lyα opacity fluctuations at very large scales in QSO absorption spectra (Becker et al. 2015; Chardin et al. 2015; Davies & Furlanetto 2016). But it may be difficult to reconcile this with measurements of the He II Lyα opacity and measurements of the IGM temperature at $z \sim 3$ (Puchwein et al. 2018; D'Aloisio et al. 2017; Madau & Haardt 2015), and also with measurements of the incidence rate of metal-line systems (Finlator et al. 2016).

Intensity mapping of atomic and molecular lines emission from galaxies in the epoch of reionization has the potential to unambiguously reveal the properties of the sources of reionization. The radiative transfer of emission in these lines in galaxies is very different from that of the Lyman-continuum emission. As a result, intensity mapping yields a view of high-redshift galaxies that is unbiased by their Lyman-continuum escape fraction. Cross-correlating this measurement with a measurement of the ionization state of the large-scale IGM, such as of the 21 cm emission or absorption from the IGM, can then result in constraints on reionizing sources.

Several experiments are currently in deployment to measure the large-scale clustering in the 21 cm signal from the IGM during the epoch of reionization, such as Murchison Widefield Array (MWA; Bowman et al. 2013; Tingay et al. 2013), Low Frequency Array (LOFAR; van Haarlem et al. 2013; Pober et al. 2014), Hydrogen Epoch of Reionization Array (HERA; Pober et al. 2014, De-Boer et al. 2016), and Square Kilometre Array (SKA; astronomers.skatelescope.org). However, 21 cm power spectrum observations alone are limited in their capability of constraining reionization parameters. This is due to the degeneracy between the Lyman-continuum escape fraction (sometimes also parameterised as the ionization efficiency) and the mass of ionizing sources: a wide range in the host halo masses of ionizing sources can produce very similar large-scale 21 cm power for a variety of escape fraction values (Greig & Mesinger 2015). Cross-correlations with other line intensity maps can potentially solve this problem by breaking the degeneracy. Our aim in this paper is to investigate this possibility.

Various emission lines have been considered in the literature as candidates for high-redshift intensity mapping, such as Lyα (Silva et al. 2013; Pullen et al. 2014), [O I] 63.2 μm and 145.5 μm (Visbal et al. 2011; Serra et al. 2016), CO(1–0) 2601 μm (Lidz et al. 2011; Gong et al. 2011), [N II] 121.9 μm and 205.2 μm (Serra et al. 2016) and [C II] 157.6 μm (Gong

et al. 2012; Silva et al. 2015; Serra et al. 2016). As these lines are a result of a reprocessing of stellar emission by the interstellar medium (Barkana & Loeb 2001; Carilli & Walter 2013), we generally expect an anti-correlation on large scales between their signal and that of the 21cm line, which originates in the neutral regions far away from galaxies (Lidz et al. 2011). The intensity mapping technique has been used at $z \sim 0.8$ using the 21 cm line (Chang et al. 2010), and at $z \sim 3$ using the [C II] (Pullen et al. 2017) and CO (Keating et al. 2016) lines. Surveys suggested for future intensity mapping include CO Mapping Pathfinder (Li et al. 2016) for CO at redshifts $z \sim 2$–3; TIME (Crites et al. 2014) and CONCERTO (Lagache 2018; Serra et al. 2016) for [C II] at redshifts $z = 5$–9; HETDEX (Hill et al. 2008) for Lyα at $z = 1.9$–3.5; SPHEREx for Lyα at redshift $z \sim 6$–8 and other lines at lower redshifts (Doré et al. 2014, 2016), and CDIM (Cooray et al. 2016) for Hα, O III, and Lyα at $z = 0.2$–10.

In this paper, we present predictions for [C II] and 21 cm brightness power spectra and the [C II]–21cm cross-power spectra from the epoch of reionization ($z = 6$–10) using a high-dynamic-range cosmological hydrodynamical simulation from the Sherwood simulation suite (Bolton et al. 2017). We forecast the sensitivity to measure these statistical quantities for the CONCERTO experiment (Lagache 2018; Serra et al. 2016) as well as a Stage II successor experiment beyond TIME and CONCERTO for [C II]. For H I, we use the experimental setups of LOFAR and SKA. Finally, we discuss the feasibility of such experiments to constrain key parameters by considering simple models of reionization. The paper is organized as follows. We first present our [C II] emission line model and 21 cm line maps in Sections 2 and 3, and then compute the cross-correlation between the [C II] and the 21 cm lines from the epoch of reionization in Section 4. We discuss the observability of the [C II] and 21 cm power spectra and the [C II]–21cm cross power spectrum in Section 5. Finally, we illustrate in Section 6 how the cross-correlation can be used to probe the nature of ionizing sources, using in particular two quantities: the minimum halo mass corresponding to a non-zero Lyman-continuum photon escape fraction and the number of ionizing photons produced by a halo. We end by summarising our results in Section 7. Our ΛCDM cosmological model has $\Omega_{\rm b} = 0.0482$, $\Omega_{\rm m} = 0.308$, $\Omega_{\Lambda} = 0.692$, $h = 0.678$, $n = 0.961$, $\sigma_8 = 0.829$, and $Y_{\rm He} = 0.24$ (Planck Collaboration 2014).

2   [C II] EMISSION FROM HIGH-REDSHIFT GALAXIES

We use a hydrodynamical cosmological simulation to model the [C II] and 21 cm signal from the epoch of reionization. This underlying simulation is identical to that used in previous work (Kulkarni et al. 2016, 2017), and is part of the Sherwood simulation suite (nottingham.ac.uk/astronomy/sherwood; Bolton et al. 2017). It has been run using the energy- and entropy-conserving TreePM smoothed particle hydrodynamical (SPH) code P-GADGET-3 that is derived from the publicly available GADGET-2 code (Springel et al. 2001; Springel 2005). We perform this simulation in a periodic, cubic volume that is 160 h^{-1}cMpc long. A large dynamic range was achieved by using a soft-

ening length of $l_{\mathrm{soft}} = 3.13\ h^{-1}\mathrm{ckpc}$, and 2048^3 dark matter and gas particles. This results in a dark matter particle mass of $M_{\mathrm{dm}} = 3.44 \times 10^7\ h^{-1}\mathrm{M}_\odot$ and gas particle mass of $M_{\mathrm{gas}} = 6.38 \times 10^6\ h^{-1}\mathrm{M}_\odot$. Initial conditions were set up at redshift $z = 99$ and evolved down to $z = 4$. We saved simulation snapshots at 40 Myr intervals between $z = 40$ and $z = 4$. In this paper, we use snapshots at $z = 6.3, 7.1, 8.2$ and 9. In order to speed the simulation up, galaxy formation is simplified by using the QUICK_LYALPHA implementation in P-GADGET-3. This converts gas particles with temperature less than 10^5 K and overdensity of more than a thousand times the mean baryon density to collisionless stars (Viel et al. 2004). Ionisation and thermal state of the gas is derived by solving for the ionization chemistry under the assumption of an equilibrium with the metagalactic UV background modelled according to Haardt & Madau (2012). The UV background of Haardt & Madau (2012) is slightly modified to result in IGM temperatures that agree with measurements by Becker et al. (2011). This chemistry solver assumes radiative cooling via two-body processes such as collisional excitation of H I, He I, and He II, collisional ionization of H I, He I, and He II, recombination, and Bremsstrahlung (Katz et al. 1996), and inverse Compton cooling off the CMB (Ikeuchi & Ostriker 1986). Metal enrichment and its effect on cooling rates is ignored. We identify dark matter haloes in the output snapshots using the friends-of-friends algorithm. In order to calculate power spectra, we project the relevant particles onto a grid to create a density field, using, in the case of gas particles, the cloud-in-cell (CIC) scheme that accounts for the SPH kernel.

If a source population at redshift z is assumed to have a line emission comoving volume emissivity $\epsilon(\nu_{\mathrm{obs}}(1 + z))$, then the specific intensity of the observed emission can be determined by solving the cosmological radiative transfer equation. The angle-averaged solution at $z = 0$ can be written as

$$I(\nu_{\mathrm{obs}}, z = 0) = \frac{1}{4\pi} \int_0^\infty dz' \frac{dl}{dz'} \frac{\epsilon(\nu_{\mathrm{obs}}(1 + z'))}{(1 + z')^3}, \qquad (1)$$

where $dl/dz = c/((1 + z)H(z))$ denotes the proper line element, and we have assumed that there is negligible absorption by the intervening intergalactic medium. Assuming an absence of contamination from other redshifts, we can model the frequency dependence by a δ-function and write

$$I(\nu_{\mathrm{obs}}, z = 0) = \frac{c}{4\pi} \frac{1}{H(z)} \frac{1}{\nu_{\mathrm{em}}(z)} \epsilon(\nu_{\mathrm{obs}}(1 + z)), \qquad (2)$$

where the $\nu_{\mathrm{em}} = \nu_{\mathrm{obs}}(1 + z)$ is the rest-frame emission frequency.

The volume-averaged emissivity ϵ is related to the line luminosity L of individual haloes by

$$\epsilon(z) = \int_{M_{\mathrm{min}}}^\infty dM \frac{dn}{dM} L_i(M, z), \qquad (3)$$

where dn/dM is the halo mass function. M_{min} is the minimum mass of haloes that can form stars and produce line emission. At $z = 7$, the minimum halo mass in our simulation is $2.3 \times 10^8\ h^{-1}\mathrm{M}_\odot$, which is close to the atomic hydrogen cooling limit. The maximum halo mass at this redshift is $3.1 \times 10^{12}\ h^{-1}\mathrm{M}_\odot$. In order to model the emissivity $\epsilon(z)$, we now need to model the halo luminosities $L(M, z)$.
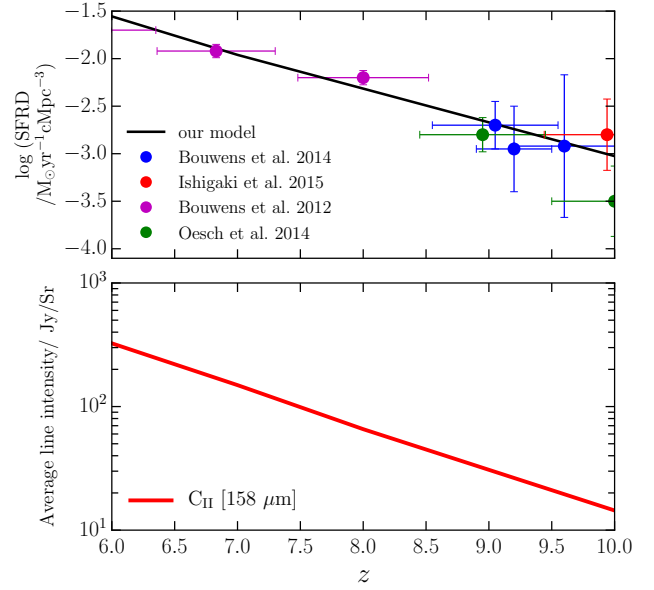
Figure 1. Top panel shows the star formation rate density evolution in our model (black curve) in comparison with various extinction-corrected observational measurements (coloured symbols). Bottom panel shows the resultant evolution of the average intensity of [C II] line emission.

2.1 Star formation rate

Linking the halo luminosities $L(M, z)$ to the star formation rate (SFR) can be done either using observational data or theoretical models of the emission processes of the different lines. The mechanism of line emission is complex; it depends on, e.g., the morphology and structure of galaxies, their metallicity, radiation field and density. Line emission can be excited by starlight, dissipation of mechanical energy by turbulence and shocks, or by the active galactic nuclei. In the reionization epoch, CMB heating and attenuation can also be important (Lagache et al. 2017). Several empirical models have been proposed for the emission of different lines, e.g., CO (Obreschkow et al. 2009; Gong et al. 2011), Lyα (Silva et al. 2013; Pullen et al. 2014; Feng et al. 2017), C II (Gong et al. 2012; Serra et al. 2016), but all of them rely on sets of poorly known parameters that characterize the galaxies and their interstellar medium in the reionization era. For the C II line, while individual galaxies have been detected at $z > 6$ (e.g., Knudsen et al. 2016; Pentericci et al. 2016; Bradač et al. 2017; Carniani et al. 2017; Strandet et al. 2017), a complete understanding of the line excitation is still lacking.

Considering the large amount of uncertainties in the detailed modelling, we will continue our study using empirical relations from the literature that relate the halo luminosity to its star formation rate (SFR) as a power law,

$$L_i \propto \mathrm{SFR}^\gamma, \qquad (4)$$

where the exponent γ encodes possible nonlinearities due to processes such as collisional excitation (Lagache et al. 2017). We assume that the SFR of a halo of mass M is proportional to the halo mass

$$\mathrm{SFR} = f_*(z) M_{\mathrm{halo}}, \qquad (5)$$

where we obtain the redshift-dependent proportionality factor by assuming a linear evolution of the log(SFRD) with redshift and calibrating $f_*(z)$ so that the resultant SFR density in the simulation box is consistent with observed data (Oesch et al. 2015). Figure 1 shows the SFR density in our model in comparison with extinction-corrected observational measurements.

2.2 CII line emission

Once we have the star formation rate model, we assign [C II] line luminosities $L_{[CII]}$ to each halo in our simulation box, by using the predicted L$_{[CII]}$–SFR relation from the model presented by Lagache et al. (2017),

$$\log \left(\frac{L_{[CII]}}{L_\odot} \right) = (1.4 - 0.07z) \times \log \left(\frac{SFR}{M_\odot yr^{-1}} \right) + 7.1 - 0.07z \,. \quad (6)$$

In this paper, the semi-analytical model (SAM) of galaxy formation G.A.S. described in Cousin et al. (2015, 2016) was used, after further modifications assuming an inertial turbulent cascade in the gas that generates a delay between the accretion of the gas and the star formation (Cousin and Guillard, submitted). It is assumed that the [C II] emission in high-z galaxies arises predominantly from photo-dominated regions (PDR). For each galaxy in the SAM, an equivalent PDR characterised by three parameters (the mean hydrogen density, gas metallicity, and interstellar radiation field) is defined. The [C II] line emission is then computed using the CLOUDY photoionisation code (Ferland et al. 2017). This model allows computation of the [C II] luminosity for a large number of galaxies (e.g., 28,000 at $z = 5$). It takes into account the effects of CMB heating and attenuation that are important at such high redshifts. The model is able to reproduce the L$_{[CII]}$–SFR relation observed for 50 star-forming galaxies at $z \geq 4$. We used here the mean relation given in Equation (6) although it is found that the L$_{[CII]}$–SFR relation is very dispersed (0.51 to 0.62 dex from $z = 7.6$ to $z = 4$). The large dispersion is due to the combined effect of different interstellar radiation fields, metallicities, and gas contents in the simulated high-redshift galaxies.

In order to calculate the three-dimensional distribution of the specific [C II] line intensity, we created coeval emission maps by assigning to each halo in the simulation volume a line luminosity $L_{[CII]}(M)$ modelled as above. Using the information about their spatial positions, we then sum the volume emissivities in each cell of a uniform 512^3 grid to obtain three-dimensional emission maps representing comoving regions of space of volume $(160 \text{ cMpc}/h)^3$. Using Equation (2), the observed specific intensity corresponding to the cell is then given by

$$I_{cell} = \frac{c}{4\pi} \frac{1}{\nu_{[CII]} H(z)} \frac{L_{[CII],cell}}{V_{cell}}, \quad (7)$$

where $L_{[CII],cell}$ is the luminosity of the cell, given by the sum of the luminosities of any haloes located in the cell. Figure 1 shows the evolution of the average line intensity. Figure 2 shows a light cone of the [C II] specific intensity created by interpolating between simulation snapshots spaced at 40 Myr intervals between $z = 6$ and 10. The simulation corresponds to a total survey area of about 1.5×1.5 deg^2,

with each cell occupying an area of $0.2' \times 0.2'$. At redshift $z = 7$, a comoving distance of 160 cMpc/h along the observation axis corresponds to about $\Delta z = 0.5$.

2.3 Power spectra

We derive three-dimensional spherically-averaged power spectra of the [C II] line emission in our model as

$$\Delta^2(k) = \frac{k^3}{2\pi^2} \cdot \frac{\langle \widetilde{I}^2(k) \rangle}{V_{box}}, \quad (8)$$

where $\widetilde{I}$ is the Fourier transform of the specific intensity defined in Equation (2), and V_{box} is the box volume, $(160 \text{ cMpc}/h)^3$. We ignore the anisotropies arising from redshift-space distortions and the redshift evolution across the box. Left column of Figure 3 shows the resultant power spectra for the [C II] emission for redshifts from $z = 6$ to 9. The shot noise contribution to the [C II] power spectrum is included. The shot noise is given by

$$\Delta^2_{shot}(k, z) = \frac{k^3}{2\pi^2} \left[\frac{c}{4\pi\nu_{[CII]} H(z)} \right]^2 \sum_i \frac{[L_{CII}(M_i, z)]^2}{V_{box}}, \quad (9)$$

where $L_{CII}(M_i, z)$ is the C II luminosity (in erg s^{-1}) of halo i with mass M_i, and the summation is over all haloes. The frequency ν_{CII} is the rest-frame frequency of the C II line. Shot noise dominates the power spectrum at $k \gtrsim 0.5 \, h/$cMpc (Serra et al. 2016), but is irrelevant in the [C II]-21cm cross power spectrum discussed in this paper, as the 21 cm emission comes from the extended IGM. Also shown in Figure 3 are the sensitivities corresponding to experimental configurations, which we discuss below.

The line emission power spectra trace the halo power spectrum, with a constant bias factor as the emission amplitude is simply proportional to the halo mass. The amplitude of the [C II] power spectrum decreases from redshift $z = 6$ to 9 by a factor of 100. Our values are consistent with those from other models in the literature (Serra et al. 2016; Silva et al. 2015; Gong et al. 2012).

3 21 CM LINE MAPS

The redshifted 21 cm signal originates in the neutral intergalactic regions. We model the brightness temperature at location $\mathbf{x}$ in our simulations in a similar manner as Kulkarni et al. (2017)

$$T_b(\mathbf{x}) = \overline{T}_b x_{HI}(\mathbf{x}) \Delta(\mathbf{x}), \quad (10)$$

where the mean temperature $\overline{T}_b \approx 22mK[(1 + z)/7]^{1/2}$ (Choudhury et al. 2009), x_{HI} is the neutral hydrogen fraction in a cell, and Δ is the gas density in units of the average density in the simulation. We neglect the impact of redshift space distortions due to peculiar velocities. We also assume that the spin temperature is much greater than the CMB temperature and that the Lyα coupling is sufficiently complete throughout the IGM.

We derive the ionization field by placing sources of Lyman-continuum radiation in dark matter haloes and using the well-known excursion set method (Furlanetto et al. 2004b; Choudhury et al. 2009; Mesinger et al. 2011). The total number of ionizing photons N_γ produced by a halo is
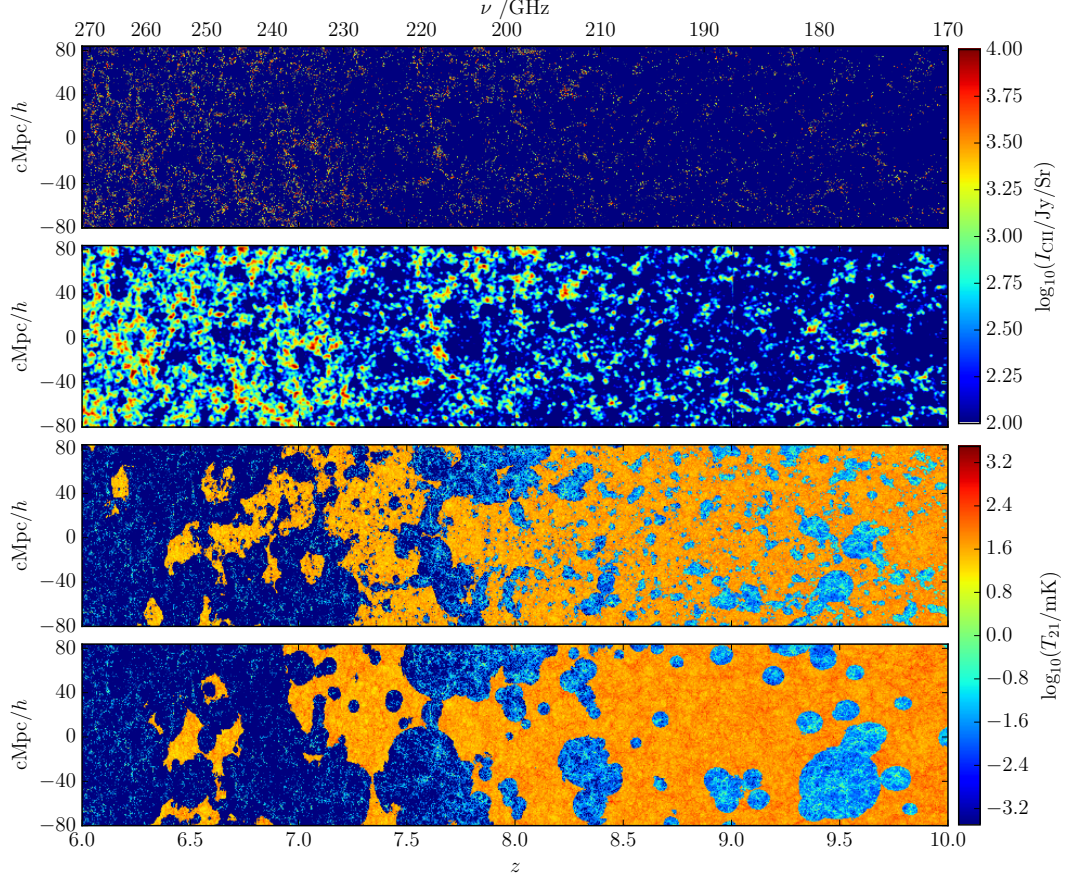
Figure 2. Light cones of [C II] and 21 cm brightness from redshift $z = 6$ to 10. The top panel shows individual sources corresponding to individual halos with mass $M_{\min} = 10^8 M_\odot$; the bottom panel shows the [C II] intensity map with a resolution of $0.4'$ (~ 1 cMpc at $z = 6$). The middle panel shows the 21 cm light cone in the reionization model with low-mass sources, while the bottom panel shows the 21 cm light cone in the reionization model with high-mass sources. The anti-correlation between the [C II] and 21 cm maps is visually apparent in the low-mass reionization model.

assumed proportional to the halo mass (Kulkarni et al. 2016)

$$N_\gamma(M) = N_\gamma^{\mathrm{LyC}} M, \tag{11}$$

where the proportionality factor N_γ^{LyC} includes the Lyman-continuum escape fraction. A grid cell at position $\mathbf{x}$ is ionized if the condition

$$\langle n_\gamma(\mathbf{x}) \rangle_R > \langle n_{\mathrm{H}}(\mathbf{x}) \rangle_R (1 + \bar{N}_{\mathrm{rec}}), \tag{12}$$

is satisfied in a spherical region centred on the cell for some radius R (Furlanetto et al. 2004a; Choudhury et al. 2009; Mesinger et al. 2011). Here, the averages are over the spherical region, n_{H} is the hydrogen number density,

$$n_\gamma = \int_{M_{\min}}^{\infty} dM \left. \frac{dN}{dM} \right|_R N_\gamma(M), \tag{13}$$

where $dN/dM|_R$ is the halo mass function within the spherical region, $M_{\min}$ is the minimum halo mass that contributes ionizing photons, and $\bar{N}_{\mathrm{rec}}$ is the average number of recombinations per hydrogen atom in the IGM. The condition in Equation (12) can be recast as

$$\zeta_{\mathrm{eff}} f(\mathbf{x}, R) \geq 1, \tag{14}$$

where the quantity

$$f = \rho_m(R)^{-1} \int_{M_{\min}}^{\infty} dM \left. \frac{dN}{dM} \right|_R M, \tag{15}$$

is the collapsed fraction into haloes of mass $M > M_{\min}$, $M_{\min}$ is the minimum mass of halos that emit Lyman continuum photons, $\rho_m(R)$ is the average matter density, and $dN/dM|_R$ is the halo mass function in the sphere of radius R. The parameter ζ_{eff} quantifies the number of photons in the IGM per hydrogen atom in stars, accounting for hydrogen recombinations in the IGM. We can write ζ_{eff} in terms of the parameters of Equations (11) and (12) as

$$\zeta_{\mathrm{eff}} = \frac{N_\gamma^{\mathrm{LyC}}}{1 - Y_{\mathrm{He}}} (1 + \bar{N}_{\mathrm{rec}})^{-1}, \tag{16}$$

where Y_{He} is the helium mass fraction. This is the only parameter that determines the ionization field in this approach. The volume-weighted ionized fraction in the simulation box is $Q_V \equiv \sum_i Q_i / n_{\mathrm{cell}}$, where the ionized volume fraction in a cell i is Q_i and n_{cell} is the total number of grid cells.

We consider two reionization models in this paper. The evolution of the ionized fraction Q_V is identical in both models, and follows the evolution in the Late/Default model of Kulkarni et al. (2016). This is achieved by solving for ζ_{eff}
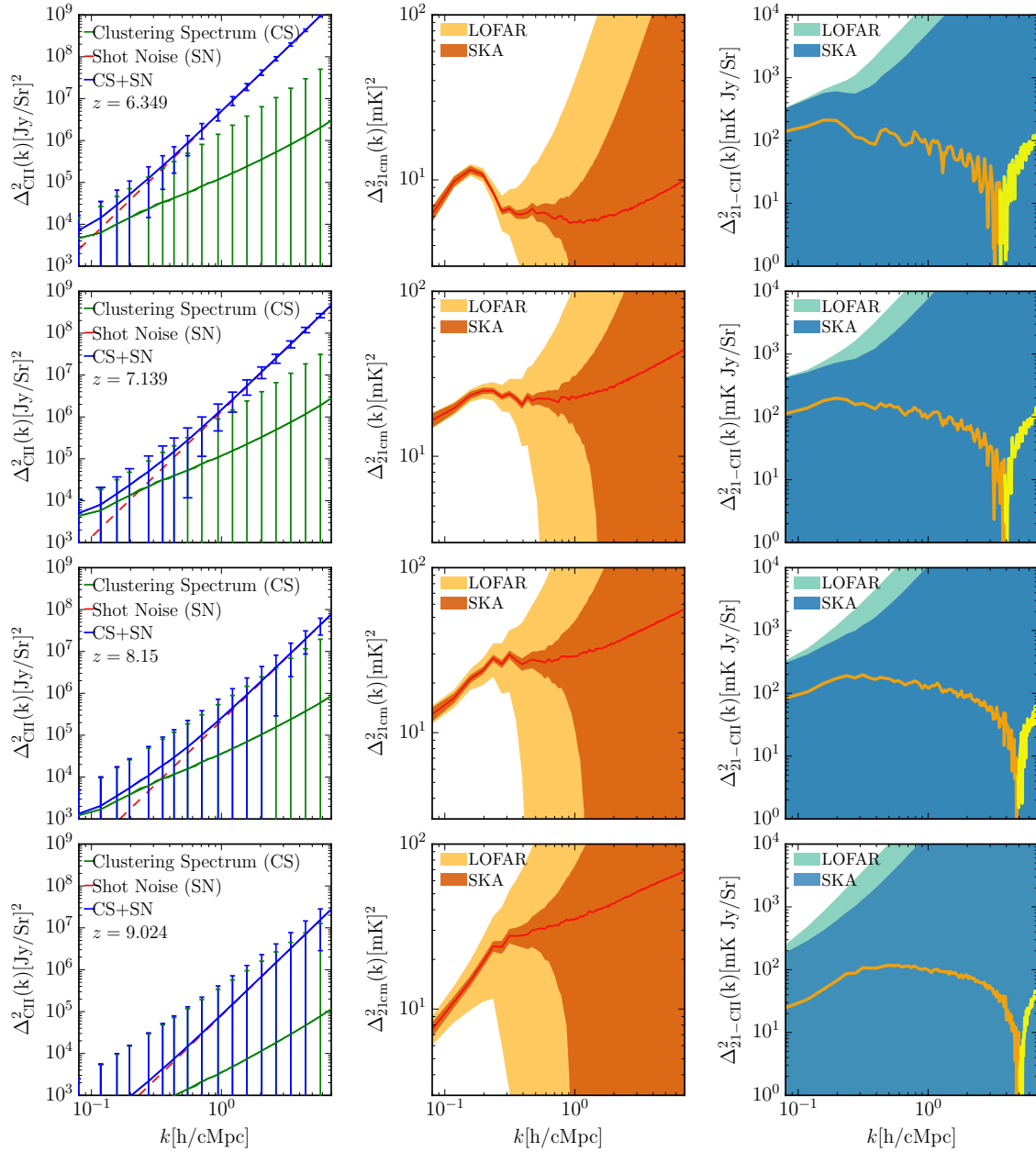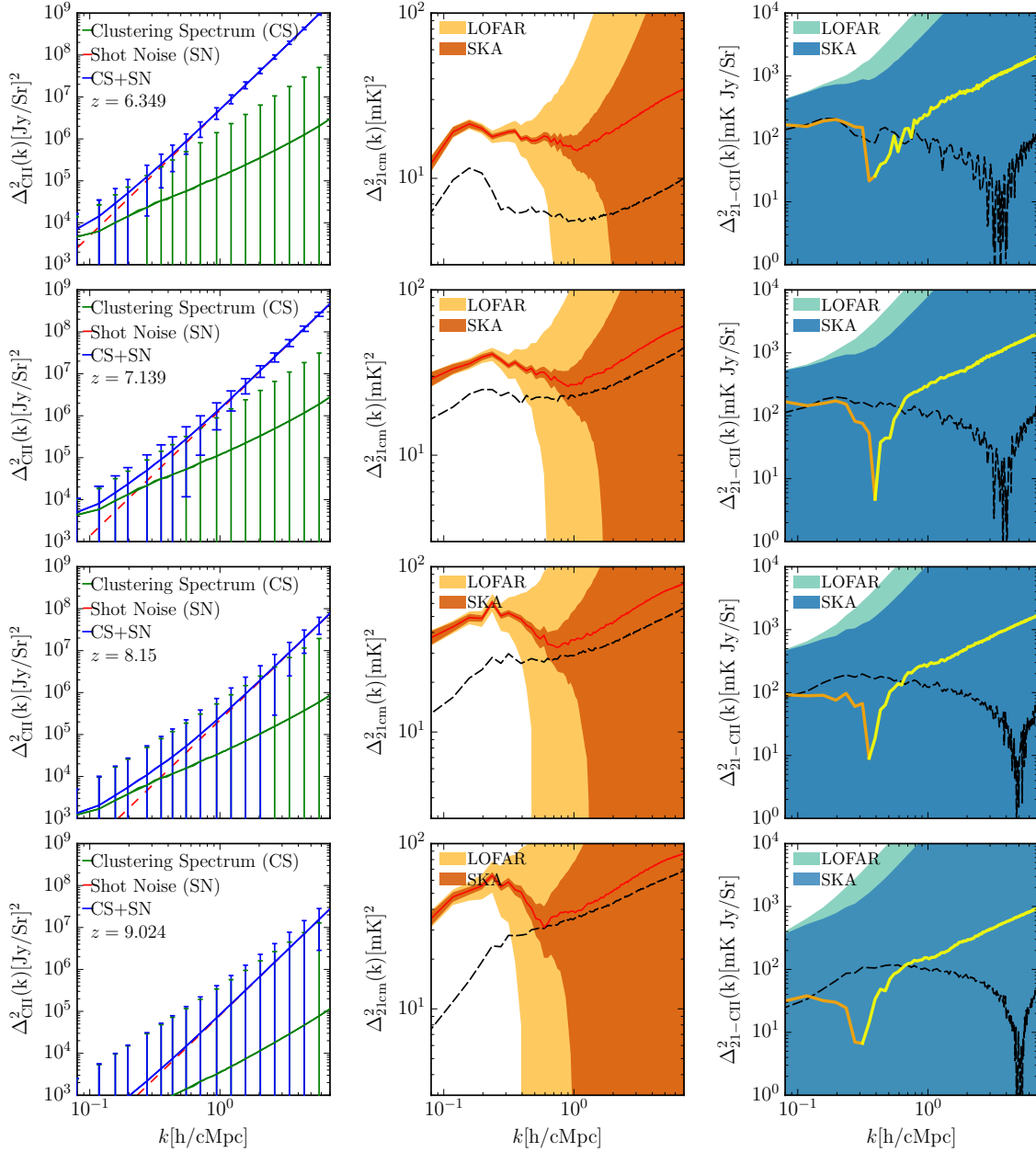
Figure 3. The [C II] power spectrum, 21 cm power spectrum, and [C II]-21cm cross power spectrum at redshifts $z = 6$–9 for the reionization model with low-mass sources. Red dashed and green solid curves in the left column show the shot noise and clustering contribution to the power spectrum, respectively. The blue curves in this column shows the total power spectrum. Error bars on the [C II] power spectra show the 1σ sensitivities for CONCERTO for $\Delta z = 0.5$ at $z = 7$, relative to the total power spectrum in blue and relative to the clustering power spectrum in green. Two sets of shaded regions show errors corresponding to LOFAR and SKA1-LOW. On the cross power spectra on the right panels, orange (yellow) lines are for negative (positive) cross-correlation coefficients.

for the assumed Q_V. The simulation box is completely ionized, i.e., $Q_V = 1$, at $z = 6$. This evolution of the ionized fraction is consistent with the constraint from the CMB measurement of the electron scattering optical depth. The two models differ however in the range of halo masses that contribute to reionizing photons. In one of the models, we set the value of the minimum halo mass in Equation (15) to be $M_{\min} = 2.3 \times 10^8$ M$_\odot$, which is approximately the mass of the smallest halo resolved in our simulation at $z = 7$. This model should represent reionization dominated by star-

forming galaxies reasonably well. In our second reionization model, we assume $M_{\min} = 10^{11}$ M$_\odot$. Only high-mass haloes contribute to reionization in this model. These reionization models with low-mass and high-mass sources present two plausible but distinct cases of source clustering, which is the quantity of interest that we want to explore later in this paper by studying its effect on the 21 cm power spectrum and the [C II]-21cm cross power spectrum.

The bottom two panels of Figure 2 show the evolution of 21 cm brightness in our two reionization models. These

Figure 4. As Figure 3 but for the reionization model with high-mass sources. The [C II] power spectra are identical to those in Figure 3. The 21 cm power spectra and the [C II]-21cm cross power spectra from Figure 3 are shown in dashed black for comparison.

light cones are analogous to those obtained for the [C II] emission, shown in the top two panels of this figure. ==Although the average ionized hydrogen fraction is the same in the two reionization models, the distribution of the 21 cm signal is quite different.== The reionization model with high-mass sources has large and more clustered ionized regions with low 21 cm brightness. More importantly, in the reionization model with low-mass sources, every source of [C II] emission is also a source of hydrogen-ionizing photons. As a result, the distribution of the 21 cm signal is anti-correlated with that of the [C II] signal: every [C II] source is located in regions with low 21 cm brightness. In the reionization model with high-mass sources, on the other hand, [C II] emitters

in haloes with masses less than $M_{\min} = 10^{11}$ M$_{\odot}$ do not contribute any hydrogen-ionizing photons. As a result, these low-mass [C II]-emitters are located in neutral regions, which are bright in 21 cm. This has an important effect on the [C II]-21cm correlation.

The middle columns of Figures 3 and 4 show the predicted 21 cm power spectra in our simulation in the reionization models with low-mass and high-mass sources, respectively. The power spectrum has a familiar shape: at small scales it is dominated by the matter power spectrum, and at large scales by a prominent "bump" due to ionized bubbles. At $k = 0.1$ $h/$cMpc the amplitude of the 21 cm power spectrum evolves from $\Delta^2(k) \sim 2$ mK^2 at $z = 9$ to 10 mK^2 at
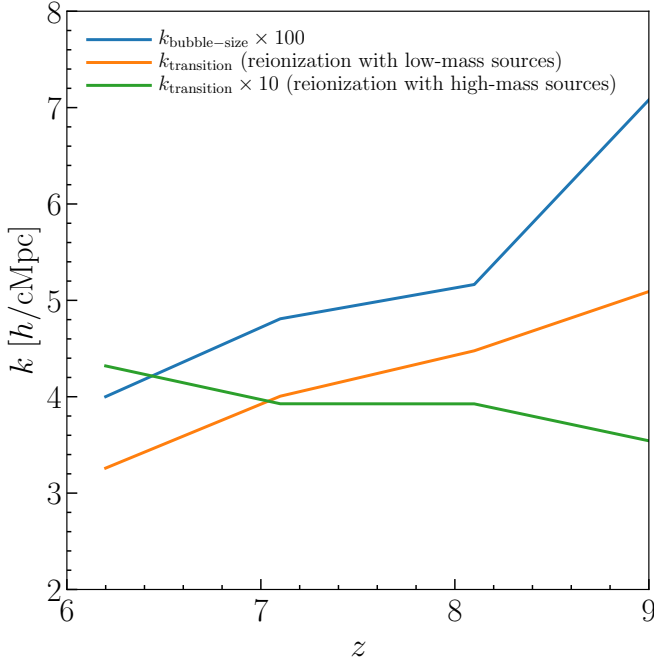
Figure 5. Evolution of the scale at which the [C II]-21cm cross power spectrum transitions from negative to positive values in the reionization model with low-mass sources (orange curve) and the reionization model with high-mass sources (green curve). The blue curve shows the evolution of the average ionized bubble size, defined simply at the the cube root of the ionized volume in the simulation box. The transition scale tracks the bubble size evolution in the model with low-mass sources, but not in the model with high-mass sources. The quantities $k_{\mathrm{bubble-size}}$ and $k_{\mathrm{transition}}$ for the high-mass reionization model have been multiplied by factors of 100 and 10, respectively, for easier comparison.

$z = 7.1$ in the reionization model with low-mass sources. In the high-mass case, the large-scale amplitude of the 21 cm power spectrum is higher, with $\Delta^2(k) \sim 35$ mK^2 at $z = 9$ to 30 mK^2 at $z = 7.1$, due to the higher clustering of ionized regions (Kulkarni et al. 2017). Figures 3 and 4 also show the sensitivity of experiments aiming to detect the 21 cm signal. We discuss this in Section 5 below.

4   THE [C II]-21CM CROSS POWER SPECTRUM

An exciting prospect for high-redshift [C II] intensity mapping is to combine it with observations of the coeval redshifted 21 cm line signal from the epoch of reionization. A detection of the [C II]-21cm cross power spectrum will assist in foreground decontamination and complement the [C II] and 21 cm power spectra as a probe of the epoch of reionization (Visbal & Loeb 2010; Lidz et al. 2011). Furthermore, the [C II]-21cm cross power spectrum may act as a direct tracer of the growth of ionizing bubbles during reionization (Gong et al. 2012).

As discussed above, Figure 2 shows light cones of the [C II] and 21 cm intensity. Typically, on large scales, we expect the [C II] emission from halos and the 21 cm signal from

the IGM to be anti-correlated, because fully neutral regions do not contain emitting galaxies, while the halo-rich regions are depleted of neutral hydrogen. On scales smaller than the ionized bubbles, however, there is positive correlation between the two fields. This behaviour is visually apparent in Figure 2, particularly at redshift $z \sim 7$, where the ionized regions are sufficiently large.

In order to study this cross-correlation quantitatively, we define the cross power spectrum of the [C II] and 21 cm intensity maps as

$$\Delta^2(k) = \frac{k^3}{2\pi^2} \cdot \frac{1}{V_{\mathrm{box}}} \cdot \frac{\langle \widetilde{I_1}^*(k)\widetilde{I_2}(k) + \widetilde{I_1}(k)\widetilde{I_2}^*(k)\rangle}{2}, \quad (17)$$

where I_1 and I_2 denote the intensities of [C II] and 21 cm, respectively. The quantity $\tilde{I}$ is the Fourier transform of I, and $\tilde{I}^*$ is the complex conjugate of $\tilde{I}$. The result is shown in the right column of Figures 3 and 4 for our reionization models with low-mass and high-mass sources, respectively. On large scales the cross-correlation is negative, as expected. In both models, at $k = 0.1$ h/cMpc, the value of the cross power spectrum is $\sim 10^2$ mK Jy/Sr at redshift $z \sim 9$. This increases to close to 5×10^2 mK Jy/Sr at $z \sim 6$. (Figures 3 and 4 also show the experimental sensitivities for measuring the cross power spectra; we discuss this in the next section.)

The scale at which the cross power spectrum transitions from positive to negative values is quite different in the two reionization models. In the low-mass model, this scale is at $k_{\mathrm{transition}} = 3$–5 h/cMpc, while it is close to $k_{\mathrm{transition}} = 0.3$ h/cMpc in the high-mass model. This is consistent with the picture that the transition scale measures the average size of ionized regions. As seen in Figure 2, the ionized regions are larger in the high-mass model, which is reflected in the value of the transition scale of the cross power spectrum. Figure 5 shows the evolution of the transition scale in the two models. The blue curve in this figure shows the evolution of the average bubble size $k_{\mathrm{bubble-size}}$ in the simulation, as measured by the cube root of the ionized volume. The evolution of the cross power spectrum transition scale in the galaxy dominated model follows that of $k_{\mathrm{bubble-size}}$, whereas the evolution in the transition scale for the high-mass model has a qualitatively different trend. This is because in the reionization model with low-mass sources, each [C II] source is also a source of hydrogen ionizing photons. Therefore, every [C II] source is in an ionized region, and there is perfect anti-correlation between the [C II] and 21 cm fields at scales larger than the bubble size. This is not the case in the high-mass reionization model, where most [C II] sources lie in neutral regions.

5   INTENSITY MAPPING EXPERIMENTS

To estimate the feasibility of [C II] intensity mapping, we consider the the CONCERTO experiment (Lagache 2018; Serra et al. 2016). We also consider a successor Stage II experiment beyond CONCERTO. The specifications for these two experiments are summarised in Table 1. Our choice of the Stage II experiment parameters is inspired by the CCAT-
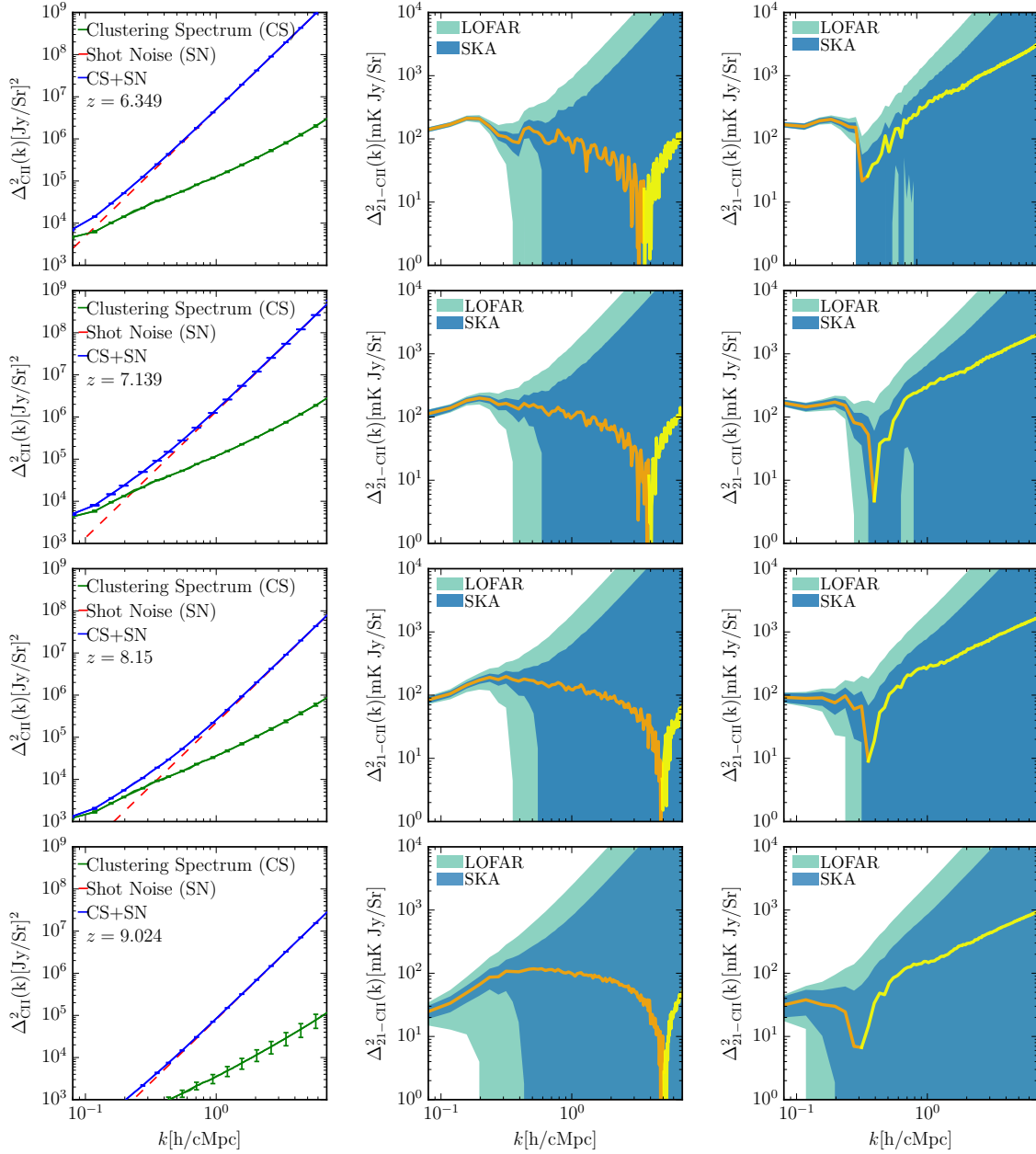
Figure 6. The [C II] power spectrum, and the [C II]-21 cm cross power spectrum for reionisation models with low-mass and high-mass sources at redshifts $z = 6$–9. Errorbars on the [C II] power spectra show sensivities for the Stage II experiment assuming a survey area of 10 deg^2 and integration time of 1000 hr. Two sets of shaded regions on the cross power spectra show errors corresponding to LOFAR and SKA surveys.

p telescope[1]. For the 21 cm signal from the same redshifts, we consider measurements using LOFAR and SKA.

5.1 [C II] experimental sensitivities

We estimate the sensitivity of experiments to measure the [C II] power spectrum by computing the uncertainty on the

power spectrum following Lidz et al. (2011); Gong et al. (2012) and Serra et al. (2016):

$$\text{var}[P_{\text{CII}}(k)] = \frac{[P_{\text{CII}}(k) + P_{\text{CII}}^{\text{N}}(k)]^2}{N_{\text{m}}(k, z)}, \qquad (18)$$

where $P_{\text{CII}}(k)$ is the model power spectrum, N_{m} is the number of modes in the survey volume with wavenumber k at redshift z, and $P_{\text{CII}}^{\text{N}}$ is the noise power spectrum. The noise power spectrum is given by

$$P_{\text{CII}}^{\text{N}} = V_{\text{pix}} \frac{\sigma_{\text{pix}}^2}{t_{\text{pix}}}, \qquad (19)$$

where V_{pix} is the volume surveyed by a single pixel, t_{pix} is the observing time per pixel, and σ_{pix}^2 is the noise variance per spectral element. The observing time per pixel is given by

$$t_{\text{pix}} = t_{\text{survey}} N_{\text{pix}} \frac{\Omega_{\text{beam}}}{A}. \tag{20}$$

Here, t_{survey} is the survey duration, which we take to be 1500 hr. The beam area Ω_{beam} is given by $\Omega_{\text{beam}} = 2\pi (\theta_{\text{beam}}/2.355)^2$, where $\theta_{\text{beam}} = 1.22\lambda_{\text{obs}}/D$ and $D = 12\,\text{m}$ for CONCERTO. We assume a survey area of $A = 2\ \text{deg}^2$. The volume surveyed by one pixel is given by (Gong et al. 2012)

$$V_{\text{pixel}}(z) = 1.1 \times 10^3 (\text{cMpc}/h)^3 \left(\frac{\lambda}{158\ \mu m} \right)$$
$$\times \left(\frac{1+z}{8} \right)^{1/2} \left(\frac{\theta_{\text{beam}}}{10\ \text{arcmin}} \right)^2 \left(\frac{\delta\nu}{400\ \text{MHz}} \right). \tag{21}$$

The noise variance σ_{pix}^2 in Equation (19) is given by

$$\sigma_{\text{pix}}^2 = \frac{\text{NEI}_{\text{diff}}^2}{N_{\text{pix}}}, \tag{22}$$

where the noise equivalent power input from diffuse emission, defined as the power from diffuse emission absorbed that produces a signal-to-noise ratio of unity at detector output, is (in MJy sr^{-1} s$^{1/2}$)

$$\text{NEI}_{\text{diff}} = \text{NEI} \times \frac{10^{-9}}{\Omega_{\text{beam}}}. \tag{23}$$

For CONCERTO, $\text{NEI}/\sqrt{N_{pix}}$=155 mJy s$^{1/2}$ (see Table 3 of Serra et al. 2016), assuming an overall transmission of the system $T = 0.3$, a spectral resolution $\delta\nu = 1.5\,\text{GHz}$, a number of pixel (and thus of spectrometer) N_{pix}=1500, a precipitable water vapor of 2 mm, an elevation of 60 degrees, and assuming the sensitivity already achieved by the NIKA2 KIDS detectors on sky (Adam et al. 2018).

The number of Fourier modes N_{m} in Equation (18) is given by

$$N_{\text{m}}(k, z) = 2\pi k^2 \Delta k \frac{V_{\text{survey}}}{(2\pi)^3}. \tag{24}$$

Here, Δk is the bin size assumed in k-space, and the survey volume is given by

$$V_{\text{survey}}(z) = 3.7 \times 10^7 (\text{cMpc}/h)^3 \left(\frac{\lambda}{158\ \mu m} \right)$$
$$\times \left(\frac{1+z}{8} \right)^{1/2} \left(\frac{A}{16\ \text{deg}^2} \right) \left(\frac{B_\nu}{20\ \text{GHz}} \right). \tag{25}$$

This allows us to estimate $\text{var}[P_{\text{CII}}(k)]$ using Equation (18). (Note that Equation (24) is approximate and may lead to an overestimated signal-to-noise ratio.) Table 1 summarises all the properties of the CONCERTO experiment.

The left columns in Figures 3 and 4 show the uncertainties in the [C II] power spectrum for the CONCERTO experiment from $z \sim 6$ to ~ 9. We find that the CONCERTO should be able to measure the large scale power spectrum of [C II] emission to redshifts of up to $z = 8$ (with a signal-to-noise ratio of ~ 1 at $k < 0.1\ h/$cMpc with 1500 hr of integration). Our predictions thus agree with the "pessimistic" case discussed by Lagache (2018).

For the Stage II experiment, we consider a noise equivalent flux density (NEFD) that is five times better than CONCERTO. We assume an aperture size of $D = 6\,\text{m}$, and a spectral resolution of $\delta\nu = 400\ \text{MHz}$. The survey duration is assumed to be $t_{\text{survey}} = 1000$ hr, while the survey area is set to $A = 10\ \text{deg}^2$. These parameters are also summarised in Table 1. The left columns in Figure 6 shows the uncertainties in the [C II] power spectrum for the Stage II experiment from $z \sim 6$–9. The signal-to-noise ratio is now enhanced by a factor of ~ 40 relative to CONCERTO at $k = 0.2\ h/$cMpc at $z = 6$. With the Stage II experiment, the power spectrum is detectable even at $z \sim 9$ with a signal-to-noise ratio of ~ 50 at $k = 0.2\ h/$cMpc.

5.2   21 cm experimental sensitivities

We study here the detectability of the 21 cm power spectrum for Low Frequency Array (LOFAR; van Haarlem et al. 2013, and the low frequency instrument from Phase 1 of the Square Kilometre Array (SKA1-LOW; astronomers.skatelescope.org). These are listed in Table 2. Similar to Equation (18), the variance of the power spectrum at mode k and redshift z is given by

$$\text{var}[P_{21}(k)] = \frac{[P_{21}(k) + P_{21}^{\text{N}}(k)]^2}{N_{\text{m}}(k, z)}. \tag{26}$$

The noise power spectrum $P_{21}^{\text{N}}(k)$ is estimated similar to Parsons et al. (2012), and is given by

$$P_{21}^{\text{N}}(k) \approx X^2 Y \frac{k^{-1/2}}{2\pi^2} \left(\frac{1}{B} \right)^{1/2} \left(\frac{1}{\Delta \ln k} \right)^{1/2}$$
$$\times \frac{\Omega}{2t} T_{\text{sys}}^2 \frac{u_{\text{max}}^{1/2}}{N} \frac{1}{\Omega^{1/4}} \frac{1}{t_{\text{per-day}}^{1/2}}, \tag{27}$$

where u_{max} is the maximum baseline b_{max} in wavelength units, and X and Y are conversion factors from angles and frequencies, respectively, to comoving distance (See Kulkarni et al. 2016 for further details). We assume $t_{\text{per-day}} = 6$ hr for 120 days. Also in Equation (27), N is the number of baselines and Ω is the field of view of an element in the array. The system temperature is assumed to be Thompson et al. (2007)

$$T_{\text{sys}} = 60\ \text{K} \left(\frac{300\ \text{MHz}}{\nu_c} \right)^{2.25}, \tag{28}$$

and calculate the thermal noise power for an integration over 120 days, assuming a bandwidth of 6 MHz, an observing time of 6 hr per day for 120 days, and a mid-latitude location.

The middle columns of Figures 3 and 4, show the resultant uncertainties in the 21 cm power spectrum for LOFAR (yellow) and SKA (brown). These experiments are only sensitive to large scales due to limited baselines. Neither of the experiments are sensitive to 21 cm power for $k \gtrsim 1\ \text{cMpc}^{-1}h$. SKA1-LOW has much greater sensitivity than LOFAR primarily due to large number of antenna elements. The signal to noise ratio is about 100 for these two experiments $k \sim 0.1$ cMpc^{-1}h. LOFAR has sensitivity for scales corresponding to $k \lesssim 0.2$ cMpc^{-1}h. At $k \sim 0.1$ cMpc^{-1}h, the signal to noise ratio for LOFAR is ~ 10.

Parameter	CONCERTO	Stage II
Aperture size (D)	12 m	6 m
Transmission (T)	0.3	0.3
Frequency window ($\Delta\nu$)	80 GHz	80 GHz
Spectral resolution ($\delta\nu$)	1.5 GHz	0.4 GHz
NEI/$\sqrt{N_{pix}}$	155 mJy s$^{1/2}$	31 mJy s$^{1/2}$
Survey area (A)	2 deg^2	10 deg^2
Survey duration (t_{survey})	1500 hr	1000 hr

Table 1. Specifications for [C II] experiments considered in this paper.

Parameter	LOFAR	SKA1-LOW
Number of antennae (N_{ant})	48	512
Effective collecting area (A_{eff})	526.0 m^2	962.0 m^2
Maximum baseline (b_{max})	3475.6 m	40286.8 m
Minimum baseline (b_{min})	22.92 m	16.8 m
Survey duration per day ($t_{\mathrm{per-day}}$)	6 hr	6 hr
Survey number of days	120	120
System temperature (T_{sys})	Equation (28)	Equation (28)

Table 2. Specifications for 21 cm experiments considered in this paper. We use SKA parameters obtained by Ghara et al. (2016) which broadly agrees with the baseline distribution given in the latest SKA1-LOW configuration document (Document number SKA-SCI-LOW-001; date 2015-10-28; http://astronomers.skatelescope.org/documents/.)

5.3 CII-21cm cross power spectrum sensitivity

We calculate the uncertainty on the cross power spectrum of [C II] with 21 cm following Gong et al. (2012),

$$\mathrm{var}[P_{\mathrm{CII},21}(k,z)] = \frac{1}{2} \left[\frac{P_{21,\mathrm{CII}}^2 + P_{21}^{\mathrm{total}}(k,z)P_{\mathrm{CII}}^{\mathrm{total}}}{N_{\mathrm{m}}(k,z)} \right], \quad (29)$$

where

$$P_{21}^{\mathrm{total}}(k,z) = P_{21}(k,z) + P_{21}^{\mathrm{N}}(k,z), \quad (30)$$

and

$$P_{\mathrm{CII}}^{\mathrm{total}}(k,z) = P_{\mathrm{CII}}(k,z) + P_{\mathrm{CII}}^{\mathrm{N}}(k,z). \quad (31)$$

The right-hand-side columns in Figures 3 and 4 show the errors on the cross power spectra for CONCERTO-LOFAR (cyan) and CONCERTO-SKA (blue) combinations. In both cases, a high signal-to-noise detection of the cross power spectrum is unlikely at least for scales smaller than $k \sim 0.1$ cMpc^{-1}h at $z = 6$–9. In the reionization model with low-mass sources, the transition scale at which the cross power spectrum changes sign is at $k \sim 5$ cMpc^{-1}h, which is out of the experimental reach. However, as discussed in the previous section, the transition scale is much larger, $k \sim 0.3$ cMpc^{-1}h, in the case of reionization by high-mass sources. This allows a detection of this scale, at least at redshifts $z = 6$ and 7. Figure 6 shows errors on the cross power spectra for LOFAR (cyan) and SKA (blue) combined with our Stage II [C II] experiment. As expected the sensivities are enhanced now to scales $k \sim 5$ cMpc^{-1}h for LOFAR and $k > 6$ cMpc^{-1}h for SKA at $z = 7$. Note that as the 21 cm signal originates in the extended IGM, the shot noise contribution to the 21 cm power spectrum and the [C II]-21cm cross power spectrum is subdominant (Kulkarni et al. 2016) and is not computed here.

6 FORECASTS FOR CONSTRAINTS

We now consider the constraints that can be obtained for astrophysical parameters related to reionization from measurements of (*a*) the 21 cm power spectrum alone, and (*b*) the 21 cm power spectrum and the [C II]-21cm cross power spectrum. A variety of astrophysical parameters determine the [C II] and 21 cm emission from the high-redshift universe. As such [C II] and 21 cm experiments can potentially constrain all of these. However, for simplicity, we consider only two parameters. We consider a scenario in which haloes down to the mass corresponding to the atomic hydrogen cooling limit $T_{\mathrm{vir}} = 10^4$ K produce [C II] emission, but only haloes with mass $M > M_{\mathrm{esc}}$ have a non-zero Lyman-continuum photon escape fraction. Our simulation resolves haloes close to the atomic hydrogen cooling limit. Thus, this scenario assumes that all haloes in our simulation are able to produce [C II] emission, but only massive haloes with mass $M > M_{\mathrm{esc}}$ participate in reionization of the IGM. The second parameter of our model is N_γ^{LyC}, which appears in Equation (11) and sets number N_γ of ionizing photons produced by a halo. Our two parameters, M_{esc} and N_γ^{LyC} thus set the minimum mass of haloes that produce ionizing photons and their Lyman-continuum brightness, respectively. The dependence of the Lyman-continuum photon escape fraction on the halo mass is not well-understood. Our choice of these parameters is therefore a simple proof of concept. Nonetheless, some simple radiative transfer models in the literature do suggest that Lyman-continuum photons are able to escape from a narrow range of halo masses (Ferrara & Loeb 2013). Our parameterisation describes this possibility.

To assess the capability of observations to constrain the parameters M_{esc} and N_γ^{LyC}, we create mock power spectra with experimental uncertainties and derive posterior probability distributions for these parameters using MCMC. This
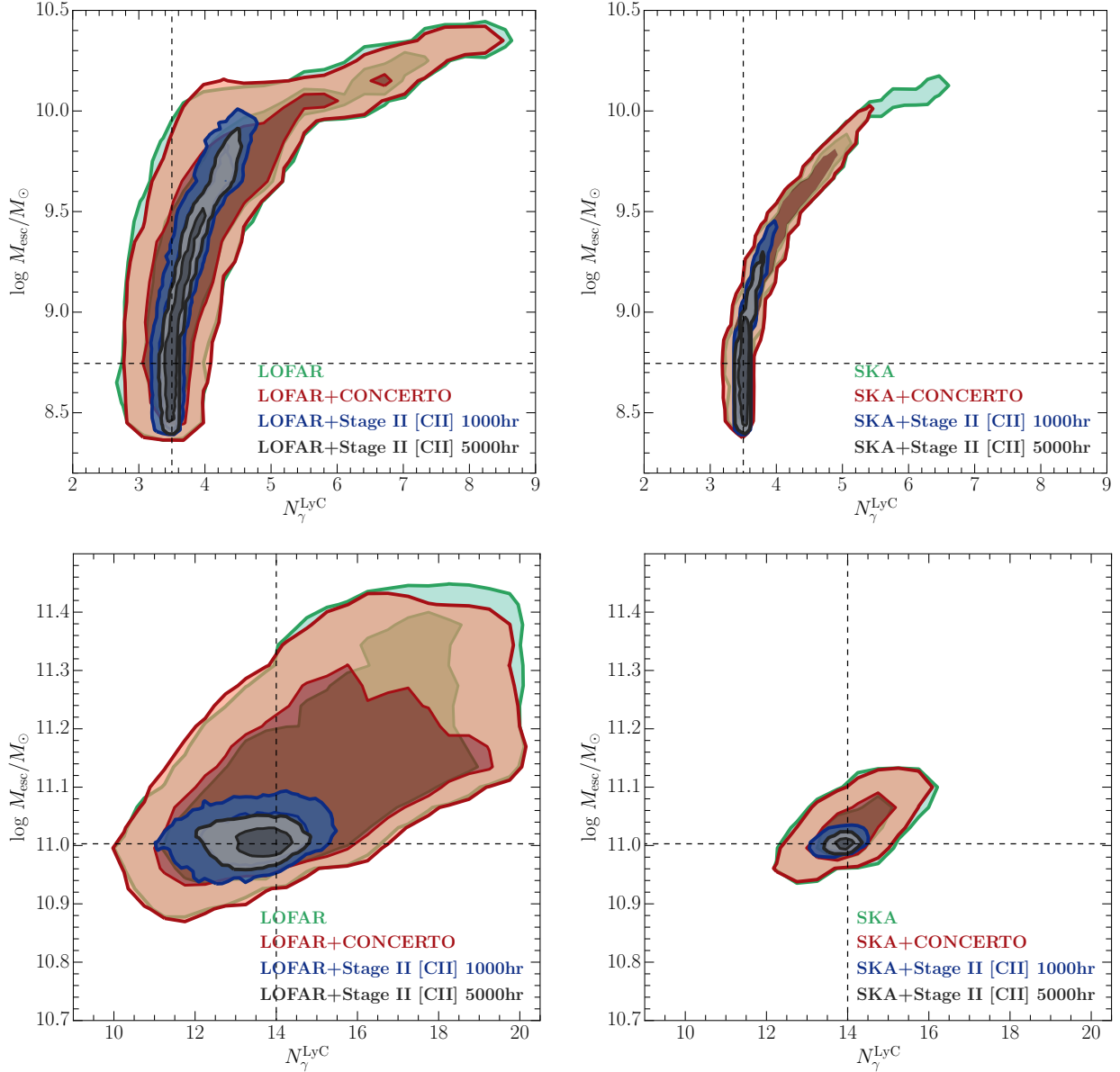
Figure 7. Constraints on astrophysical parameters from mock measurements of the 21 cm power spectrum and the [C II]-21cm cross power spectrum. Panels in the top row describe the reionization scenario with low-mass sources, and those in the bottom row describe the reionization scenario with high-mass sources. The two panels in each case refer to the use of LOFAR and SKA for the 21 cm power spectrum measurement. The dashed lines show the location of the "true" values of the parameters. The green contours show the 1σ and 2σ constraints when only 21 cm power spectrum data is used. Contours in other colours show constraints obtained when the [C II]-21cm cross power spectrum data is added to the analysis.

approach is similar to that considered, for instance, for 21 cm experiments by Greig & Mesinger (2015). We consider two mock observations of the 21 cm power spectrum and the [C II]-21cm cross power spectrum. In one of these mocks, our two parameters have values $M_{\rm esc} = 5.56 \times 10^8$ M$_\odot$ and $N_\gamma^{\rm LyC} = 3.5$. This corresponds to the power spectra shown in Figure 3. The associated uncertainties are also those shown in Figure 3. For the second mock observation, the mock measurements and associated errors are the power spectra shown in Figure 4. This mock data has $M_{\rm esc} = 10^{11}$ M$_\odot$ and $N_\gamma^{\rm LyC} = 14$. As the shot noise dominates the total power, we only fit the clustering power spectrum in this exercise.

For each of the mock datasets, we infer the posterior distributions for $M_{\rm esc}$ and $N_\gamma^{\rm LyC}$ by writing a Gaussian likelihood for the data as

$$\log \mathcal{L}(\Delta^2 | M_{\rm esc}, N_\gamma^{\rm LyC}) \propto -\frac{1}{2} \sum_i \log\left(2\pi\sigma^2(k_i)\right)$$
$$- \sum_i \frac{(\Delta^2_{\rm mock}(k_i) - \Delta^2_{\rm model}(k_i, M_{\rm esc}, N_\gamma^{\rm LyC}))^2}{2\sigma^2(k_i)}, \quad (32)$$

where Δ^2 denotes the power spectrum or the cross-power spectrum, as the case may be, the index i runs over the k-bins, and σ is the error on the mock observation at wavenumber k_i, estimated for various experiments following the pro-

cedure described in Sections 5.1 and 5.2. We then explore the capability of our model to identify the parameters used to create the mock data, by inferring the values of these parameters in a Bayesian fashion. We use Markov Chain Monte Carlo to sample the posterior distributions of the parameters, using a modified version of the 21 cm inference code 21CMMC (Greig & Mesinger 2015) to derive distributions for the parameters M_{esc} and $N_{\mathrm{min}}^{\mathrm{LyC}}$ assuming wide, uniform priors. For given values of the parameters, we compute $\Delta_{\mathrm{model}}^2$ by first running our simulation (as described in Section 2 and Section 4; with the power spectrum and cross power spectrum as defined in Equations 8 and 17) over a grid of points in the parameter space and then linearly interpolating between the values of the likelihood to get it at an arbitrary parameter value. Our grid of models has 399 simulations. It spans 19 values of $N_{\mathrm{min}}^{\mathrm{LyC}}$ and 21 values of M_{esc}.

The resultant posterior joint probability distributions are shown in Figure 7. Panels in the top row describe the low-mass reionization scenario, and those in the bottom row describe the high-mass reionization scenario. The two panels in each case refer to the use of LOFAR and SKA for the 21 cm power spectrum measurement. The dashed lines show the location of the "true" values of the parameters, which were used to produce the mock data. The green contours show the 1σ and 2σ constraints when only 21 cm power spectrum data is used. In this case, there is a strong degeneracy in the two parameters in the low-mass reionization scenario. This degeneracy persists in the high-mass case, although its magnitude is considerably reduced. Constraints in the high-mass case are good even with the 21 cm data alone, as the power spectrum has an enhanced amplitude in this case, which allows for a high signal-to-noise measurement. Contours in other colours in Figure 7 show constraints obtained when the [C II]-21cm cross power spectrum data is added to the analysis. We find that this considerably improves the constraints for the Stage II [C II] experiment. With data from 1000 hr and 5000 hr of the Stage II experiment, the improvement in 1σ constraints on M_{esc} relative to 21 cm measurements is by factors of 3 and 10 respectively. The improvement is of a comparable magnitude in the high-mass case. The constraints also show a modest improvement when SKA measurements are considered instead of LOFAR. Due to low signal-to-noise, 1500 hr data from CONCERTO do not result in a significant improvement in the constraints.

7 CONCLUSIONS

We have outlined the prospects of intensity mapping the epoch of reionization using the redshifted 21 cm line and the [C II] emission line from high-redshift galaxies. We have modelled the galaxy line emissions using a semi-analytical model. Using a high dynamic range cosmological simulation, we found that on large scales of $\gtrsim 60$ cMpc/h at redshift $z = 6$ the spherically averaged power spectrum of the [C II] line emission have values of $\Delta^2 \sim 10^5$ $(\mathrm{Jy/sr})^2$ at $k \sim 0.2$ h/cMpc. This value reduces to about 10^3 $(\mathrm{Jy/sr})^2$ at $z \sim 9$.

We find that the [C II] power spectrum predicted in our model should be detectable with the CONCERTO experiment up to $z \sim 8$ with a signal-to-noise ratio of $\gtrsim 1$ at

$k = 0.2$ h/cMpc. A Stage-II experiment with five times better sensitivity than CONCERTO should be able to detect the [C II] power spectrum at even higher redshifts. The cross power spectrum of the [C II] and coeval 21 cm signal from the epoch of reionization would be valuable in many ways. The scale at which this cross power spectrum changes sign can contain the average size of ionized regions, at least when the sources of reionization coincide with the galaxies that produce the [C II] signal. A detection of this cross power spectrum could help in the removal of low-redshift foregrounds from the 21 cm data. The cross power spectrum will also provide constraints on important astrophysical parameters. We have investigated the capability by analysing mock 21 cm power spectrum data and [C II]-21cm cross power spectrum data in a Bayesian way to derive constraints under various experimental assumptions. We find that [C II]-21cm correlation measurements can improve constraints on the mass of reionization sources by factors of 3–10 beyond constraints from 21 cm experiments alone.

REFERENCES

Adam R., et al., 2018, A&A, 609, A115
Barkana R., Loeb A., 2001, Phys. Rep., 349, 125
Becker G. D., Bolton J. S., Haehnelt M. G., Sargent W. L. W., 2011, MNRAS, 410, 1096
Becker G. D., Bolton J. S., Madau P., Pettini M., Ryan-Weber E. V., Venemans B. P., 2015, MNRAS, 447, 3402
Bolton J. S., Puchwein E., Sijacki D., Haehnelt M. G., Kim T.-S., Meiksin A., Regan J. A., Viel M., 2017, MNRAS, 464, 897
Boutsia K., et al., 2011, ApJ, 736, 41
Bowman J. D., et al., 2013, Publ. Astron. Soc. Australia, 30, e031
Bradač M., et al., 2017, ApJ, 836, L2
Carilli C. L., 2011, ApJ, 730, L30
Carilli C. L., Walter F., 2013, ARA&A, 51, 105
Carniani S., et al., 2017, A&A, 605, A42
Chang T.-C., Pen U.-L., Bandura K., Peterson J. B., 2010, Nature, 466, 463
Chardin J., Haehnelt M. G., Aubert D., Puchwein E., 2015, MNRAS, 453, 2943

Choudhury T. R., Haehnelt M. G., Regan J., 2009, MNRAS, 394, 960

Cooray A., et al., 2016, preprint, arXiv:1602.05178 [astro-ph.CO]

Cousin M., Lagache G., Bethermin M., Blaizot J., Guiderdoni B., 2015, A&A, 575, A32

Cousin M., Buat V., Boissier S., Bethermin M., Roehlly Y., Génois M., 2016, A&A, 589, A109

Crites A. T., et al., 2014, in Millimeter, Submillimeter, and Far-Infrared Detectors and Instrumentation for Astronomy VII. p. 91531W, doi:10.1117/12.2057207

D'Aloisio A., Upton Sanderbeck P. R., McQuinn M., Trac H., Shapiro P. R., 2017, MNRAS, 468, 4691

Davies F. B., Furlanetto S. R., 2016, MNRAS, 460, 1328

DeBoer D. R., et al., 2016, preprint, arXiv:1606.07473 [astro-ph.IM]

Doré O., et al., 2014, preprint, arXiv:1412.4872 [astro-ph.CO]

Doré O., et al., 2016, preprint, arXiv:1606.07039 [astro-ph.CO]

Fan X., et al., 2006, AJ, 132, 117

Feng C., Cooray A., Keating B., 2017, ApJ, 846, 21

Ferland G. J., et al., 2017, Rev. Mex. Astron. Astrofis., 53, 385

Ferrara A., Loeb A., 2013, MNRAS, 431, 2826

Finkelstein S. L., 2016, Publ. Astron. Soc. Australia, 33, e037

Finlator K., Oppenheimer B. D., Davé R., Zackrisson E., Thompson R., Huang S., 2016, MNRAS, 459, 2299

Fonseca J., Silva M. B., Santos M. G., Cooray A., 2017, MNRAS, 464, 1948

Furlanetto S. R., Zaldarriaga M., Hernquist L., 2004a, ApJ, 613, 1

Furlanetto S. R., Zaldarriaga M., Hernquist L., 2004b, ApJ, 613, 16

Ghara R., Choudhury T. R., Datta K. K., 2016, MNRAS, 460, 827

Giallongo E., et al., 2015, A&A, 578, A83

Gong Y., Cooray A., Silva M. B., Santos M. G., Lubin P., 2011, ApJ, 728, L46

Gong Y., Cooray A., Silva M., Santos M. G., Bock J., Bradford C. M., Zemcov M., 2012, ApJ, 745, 49

Gong Y., Cooray A., Santos M. G., 2013, ApJ, 768, 130

Grazian A., et al., 2016, A&A, 585, A48

Greig B., Mesinger A., 2015, MNRAS, 449, 4246

Haardt F., Madau P., 2012, ApJ, 746, 125

Hill G. J., et al., 2008, in Kodama T., Yamada T., Aoki K., eds, Astronomical Society of the Pacific Conference Series Vol. 399, Panoramic Views of Galaxy Formation and Evolution. p. 115 (arXiv:0806.0183 [astro-ph])

Ikeuchi S., Ostriker J. P., 1986, ApJ, 301, 522

Japelj J., et al., 2017, MNRAS, 468, 389

Katz N., Weinberg D. H., Hernquist L., 1996, ApJS, 105, 19

Keating G. K., Marrone D. P., Bower G. C., Leitch E., Carlstrom J. E., DeBoer D. R., 2016, ApJ, 830, 34

Khaire V., Srianand R., Choudhury T. R., Gaikwad P., 2016, MNRAS, 457, 4051

Knudsen K. K., Richard J., Kneib J.-P., Jauzac M., Clément B., Drouart G., Egami E., Lindroos L., 2016, MNRAS, 462, L6

Kulkarni G., Choudhury T. R., Puchwein E., Haehnelt M. G., 2016, MNRAS, 463, 2583

Kulkarni G., Choudhury T. R., Puchwein E., Haehnelt M. G., 2017, MNRAS, 469, 4283

Lagache G., 2018, preprint, arXiv:1801.08054 [astro-ph.GA]

Lagache G., Cousin M., Chatzikos M., 2017, preprint, (arXiv:1711.00798)

Li T. Y., Wechsler R. H., Devaraj K., Church S. E., 2016, ApJ, 817, 169

Lidz A., Furlanetto S. R., Oh S. P., Aguirre J., Chang T.-C., Doré O., Pritchard J. R., 2011, ApJ, 741, 70

Livermore R. C., Finkelstein S. L., Lotz J. M., 2017, ApJ, 835, 113

Madau P., Haardt F., 2015, ApJ, 813, L8

Majumdar S., Mellema G., Datta K. K., Jensen H., Choudhury T. R., Bharadwaj S., Friedrich M. M., 2014, MNRAS, 443, 2843

McQuinn M., Zahn O., Zaldarriaga M., Hernquist L., Furlanetto S. R., 2006, ApJ, 653, 815

Mesinger A., Furlanetto S., Cen R., 2011, MNRAS, 411, 955

Micheva G., Iwata I., Inoue A. K., Matsuda Y., Yamada T., Hayashino T., 2017, MNRAS, 465, 316

Mostardi R. E., Shapley A. E., Steidel C. C., Trainor R. F., Reddy N. A., Siana B., 2015, ApJ, 810, 107

Obreschkow D., Croton D., De Lucia G., Khochfar S., Rawlings S., 2009, ApJ, 698, 1467

Oesch P. A., Bouwens R. J., Illingworth G. D., Franx M., Ammons S. M., van Dokkum P. G., Trenti M., Labbé I., 2015, ApJ, 808, 104

Oesch P. A., et al., 2016, ApJ, 819, 129

Ota K., et al., 2017, ApJ, 844, 85

Parsons A., Pober J., McQuinn M., Jacobs D., Aguirre J., 2012, ApJ, 753, 81

Pentericci L., et al., 2016, ApJ, 829, L11

Planck Collaboration 2014, A&A, 571, A16

Planck Collaboration 2016, A&A, 596, A108

Pober J. C., et al., 2014, ApJ, 782, 66

Pritchard J. R., Loeb A., 2012, Reports on Progress in Physics, 75, 086901

Puchwein E., Haardt F., Haehnelt M. G., Madau P., 2018, preprint, arXiv:1801.04931 [astro-ph.GA]

Pullen A. R., Doré O., Bock J., 2014, ApJ, 786, 111

Pullen A. R., Serra P., Chang T.-C., Dore O., Ho S., 2017, preprint, arXiv:1707.06172 [astro-ph.CO]

Robertson B. E., Ellis R. S., Furlanetto S. R., Dunlop J. S., 2015, ApJ, 802, L19

Serra P., Doré O., Lagache G., 2016, ApJ, 833, 153

Siana B., et al., 2015, ApJ, 804, 17

Silva M. B., Santos M. G., Gong Y., Cooray A., Bock J., 2013, ApJ, 763, 132

Silva M., Santos M. G., Cooray A., Gong Y., 2015, ApJ, 806, 209

Springel V., 2005, MNRAS, 364, 1105

Springel V., Yoshida N., White S. D. M., 2001, New Astron., 6, 79

Strandet M. L., et al., 2017, ApJ, 842, L15

Suginohara M., Suginohara T., Spergel D. N., 1999, ApJ, 512, 547

Thompson A. R., Moran J. M., Swenson G. W., 2007, Interferometry and Synthesis in Radio Astronomy, John Wiley & Sons, 2007.

Tingay S. J., et al., 2013, Publ. Astron. Soc. Australia, 30, e007

Vanzella E., et al., 2010, ApJ, 725, 1011

Viel M., Haehnelt M. G., Springel V., 2004, MNRAS, 354, 684

Visbal E., Loeb A., 2010, J. Cosmology Astropart. Phys., 11, 016

Visbal E., Trac H., Loeb A., 2011, J. Cosmology Astropart. Phys., 8, 010

Yue B., Ferrara A., Pallottini A., Gallerani S., Vallini L., 2015, MNRAS, 450, 3829

van Haarlem M. P., et al., 2013, A&A, 556, A2

This paper has been typeset from a TEX/LATEX file prepared by the author.